Photonic Metamaterial with Sub-Wavelength Electrode Pattern

GUILLAUME CROES[1,2,4], RENAUD PUYBARET[1], JANUSZ BOGDANOWICZ[1], UMBERTO CELANO[1,3], ROBERT GEHLHAAR[1] AND JAN GENOE[1,2]

[1] *imec, Sensors and Actuators Technology (SAT) Dept., Kapeldreef 75, 3001 Leuven, Belgium*

[2] *Electrical Engineering Dept. (ESAT), Katholieke Universiteit Leuven, 3001 Leuven, Belgium*

[3] *School of Electrical, Computer and Energy Engineering, Arizona State University, Tempe, AZ, 85287 USA*

[4] *Guillaume.Croes@imec.be*

https://orcid.org/0000-0001-6168-9794

Abstract: The next generation of tunable photonics require highly conductive and light inert interconnects that enable fast switching of phase, amplitude and polarization modulators without reducing their efficiency. As such, metallic electrodes should be avoided as they introduce significant parasitic losses. Transparent conductive oxides, on the other hand, offer reduced absorption due to their high bandgap and good conductivity due to their relatively high carrier concentration. Here, we present a metamaterial that enables electrodes to be in contact with the light active part of optoelectronic devices without the accompanying metallic losses and scattering. To this end, we use transparent conductive oxides and refractive index matched dielectrics as the metamaterial constituents. We present the metamaterial construction together with various characterization techniques that confirm the desired optical and electrical properties.

1. Introduction

Large area photonic devices as metasurfaces, optical phased arrays and spatial light modulators (SLM) have shown excellent control over incident light, whether waveguide fed or plane wave illuminated. Their large degree of freedom is unique and enabled them to bring new perspectives to applications such as wavefront shaping and holography. [1] They achieve these feats due to careful design of the modulators that influence phase, amplitude and polarization. Evidently, a vast array of technologies including thermo-optics [2], microelectromechanical systems [3, 4], liquid crystals [5, 6] and phase change materials [7, 8] are being explored to enable fast and reliable modulator switching. Some of these state-of-the-art devices, such as metasurfaces, cannot be switched, while others are currently controlled optically. [9, 10] In either case, electrical modulation is preferred for more robust switching. However, even when devices are electrically tunable, doing this over a large area remains a challenge due to the combination of electrode losses and desired modulator size. This is due to the link between the attainable field of view and the modulator or pixel size, which states that accurate control spanning over a 180° viewing angle requires subwavelength modulation. Hence, factoring in the refractive index of the modulator, light modulation needs to occur at scale of 100nm or less. Consequently, a similar size restriction exists for the accompanying driving electronics needed to individually address each modulator. Due to the shear number ($> 1E7/mm^2$) of modulators that need switching, the most common approach would be to create metallic interconnects which introduce significant parasitic losses into the devices, leading to reduced efficiency.

It is well known that metallic electrodes can impede the operation of photonic, optoelectronic and plasmonic devices such as LEDs, liquid crystal cells and waveguide modulators due to their strong light matter interaction. [11, 12] This behaviour stems from their high carrier concentration,
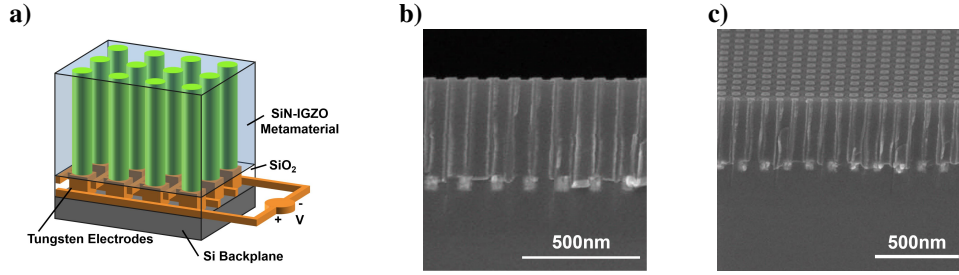
Fig. 1. a) Schematic of the metamaterial. b) Cross section SEM image. c) Angled top down SEM image.

which leads to a high conductivity but also to a high absorption due to the unbound nature of conduction electrons. The lowered performance can be avoided by taking special care with the device design. In practice, this often results in physically separating the metal from the active region which is not an ideal solution for high modulator densities. Alternatively, a wide range of materials are being considered to replace metals as electrode including transparent conducting oxides (TCOs) and diluted metals. [13–16]

Transparent conductive oxides form a group of materials that are easily deposited, CMOS compatible, highly optically tunable [17] and have carrier densities similar to highly doped semiconductors [18], hence well below those of metals. On top of that, they are semi-transparent to transparent due to their high bandgap and have been extensively used in thin film devices as LEDs and touch screens. Nowadays, these material are becoming more widespread, finding uses in metasurfaces [19–22], epsilon near zero materials [23–25] and electro-optical modulators [26–28]. TCOs are often used in tandem with metals due to their non-negligible ohmic losses. Hence, they typically form a bridge between the light active region of the device and the peripheral electrical circuitry. However, in periodic structures, such as tunable metasurfaces and spatial light modulators, TCOs are typically not index matched with their surrounding materials. This again leads to undesired scattering of incident light, depending on the grating formed by the periodic TCO.

Here, we present a metamaterial that employs a TCO together with an index matched dielectric such that electric bias can be applied directly to the active light region. Additionally, this metamaterial can be used as cladding layer in integrated photonics since the material optically behaves isotropic in the chosen light range. The employed electrode scale allows sub-wavelength and individual electrode modulation in the visible range resulting in a 180° viewing angle without any ghost images or scattering artefacts. Consequently, the created metamaterial enables the creation of high-density tunable modulators for transmission, reflection or waveguide based applications such as a holographic display. We showcase the required fabrication techniques and give insight in the optical and electrical properties by ellipsometry, scatterometry, Rigorous Coupled Wave Analysis (RCWA) and Conductive Atomic Force Microscopy (C-AFM).

2. Metamaterial Design and Fabrication

A metamaterial was designed to provide the electrical bias required for a waveguide based spatial light modulator. To that end, three criteria where kept in mind. Namely: (1) steering over a 180° range is enabled, (2) no light scattering due to a refractive index difference between the electrode and dielectric material, and (3) no or limited influence from the remaining metallic components.

Firstly, ensuring a device can steer over the full 180° range requires a modulation at half the size of the desired wavelength. (Diffraction Grating) However, since the envisioned device is waveguide-based, the required modulation is linked to the internal wavelength. Hence, it is the effective refractive index of the guided mode of the envisioned SLM that determines the pitch of these sub-wavelength electrodes. A well confined mode calls for a waveguide refractive index that is higher than the cladding materials. For common strong electro-optic materials, such as Lithium Niobate ($LiNbO_3$) and Barium Titanate ($BaTiO_3$) an electrode pitch of 90nm practically covers the entire visible spectrum. [29–31]

Secondly, it is the optical properties of the constituent materials of the metamaterial that determine whether Bragg scattering can occur. Figure 1 a) shows a schematic of the envisioned metamaterial. Several TCO's were considered, including Indium Tin Oxide (ITO), Aluminum doped Zinc Oxide (Al:ZnO) and Indium Gallium Zinc Oxide (IGZO). Since atomic layer deposition (ALD) was needed for uniform filling, only ITO and IGZO were at hand in our fab. IGZO was preferred over ITO since it is known to have a lower intrinsic carrier concentration which suits the intended application, as it does not require high switching speeds (video rate) while simultaneously lowering parasitic absorption. For other applications, such as optical I/O, ITO can result in faster switching at the cost of slightly higher optical losses. Silicon Nitride (SiN) was paired to IGZO as dielectric since it is semiconductor fab compatible, easily deposited and tunable over the same refractive index range. We used an IGZO recipe which has proven to yield good conductivity, to which we index matched SiN to ensure the desired electrical properties. [32, 33] This is beneficial since at wavelengths where both refractive indices match, their combination will behave isotropic. On top of that, even if a small refractive index difference exists, the small electrode pitch leads to reduced Bragg scattering since only higher order and thus weaker scattering can take place.

Finally, to limit undesired absorption from metallic backplane components, the metamaterial is preferred as thick as possible to separate the waveguide physically from any metals. However, for ease of manufacturing the aspect ratio (AR) (depth/width) of the electrode pillars cannot be excessively large. The metamaterial was thus made 500nm thick, resulting in an easily reproducible metamaterial with AR close to 11.

In practice, the metamaterial waveguide cladding layer is created as follows. First, a TiN / Tungsten back contact on SiOx with critical dimension 50nm is created using a damascene process : 300nm SiOx deposition on Si substrate, lithography 193nm immersion with BARC and positive-tone resist, 100nm etch of SiOx, 10nm TiN ALD, 200nm W fill, CMP for planarization. Afterwards, the metamaterial is created by depositing a thick SiN layer (500nm) which is then subjected to a high AR etch to open 45nm sized holes with 90nm pitch. Atomic layer deposition (ALD) is subsequently used to fill the SiN holes. Due to ALD's structure filling capabilities a conformal IGZO fill can be achieved along the whole pillar as shown in Figure 1 b) - c). Chemical-Mechanical Polishing (CMP) is used to remove the excess IGZO from the top and planarize the metamaterial. During planarization, a small amount of the metamaterial is consumed, resulting in a layer thickness around 420nm. This entire process is done in imec's CMOS 300mm fab. A post-process anneal in an O_2 rich environment at 250°C for an hour enables the IGZO conductivity through the creation of oxygen vacancies. [34]

3.   Results and Discussion

3.1.   *Optical Characterization*

Optical characterization was performed on planar layers (Ellipsometry) and on the finished metamaterial (Scatterometry and RCWA) to gain insight their refractive indices and structural parameters respectively.

3.1.1.   Ellipsometry

The optical properties of the constituent materials are shown in Figure 2 a) - b). Ellipsometric measurements (Woollam RC2) were performed on planar layers after which the data was fitted using a Tauc-Lorentz oscillator for SiN and a combination of Tauc-Lorentz and Drude oscillators for IGZO and the metamaterial. Here, the Tauc-Lorentz oscillator represents the amorphous nature of both SiN and IGZO, and the Drude oscillator is employed to fit IGZO's metallic infrared absorption. [35, 36].

To limit the present degrees of freedom, as both IGZO and SiN are highly tunable materials depending on their deposition parameters, a previously optimized recipe for high conductivity IGZO was used. [32, 33] The fitting parameters for IGZO can be found in Table 1. Its resistivity, $0.003681\Omega cm$, extracted from the Drude oscillator is similar to the resistivity of a weakly conducting semiconductor. This approach ensures the desired electrical properties and only requires SiN to be varied by altering its deposition parameters, influencing its stoichiometry and density, until its real refractive index matches well in the visible (440nm-640nm) as indicated in Figure 2 a) and b). Thus limiting the number of required blanket wafers. The total measured SiN range (light blue) as well as the closest matching SiN wafer (black) is shown in Figure 2 a) and b). Its fitting parameters are shown in Table 2. All ellipsometry measurements, including the full SiN range can be found in Data File 1.

Table 1. SiN fitting parameter for the employed Tauc-Lorentz oscillator.

SiN Tauc Lorentz Parameter	Amp (eV)	Eo (eV)	Br (eV)	Eg (eV)
Value	57.5564	7.422	5.951	2.654

Table 2. IGZO fitting parameters for a Tauc-Lorentz and Drude oscillator model.

IGZO Tauc Lorentz Parameter	Amp (eV)	Eo (eV)	Br (eV)	Eg (eV)
Value	118.5894	3.540	11.140	3.163
IGZO Drude Parameter	Resistivity (Ω cm)		Scattering time (fs)	
Value	0.003681		2.096	

The completed metamaterial was initially fitted with the 3 oscillators expected for a blend of both materials (2 Tauc-Lorentz and 1 Drude) and constrained to a thickness of 420nm measured by SEM. Unfortunately, this model does not result in a good fit as one of the Tauc-Lorentz oscillators yields unrealistic values. The best possible fit, shown in Table 1 of the Supplemental Document, was achieved by using only one Tauc-Lorentz oscillator, for which the refractive indices are shown
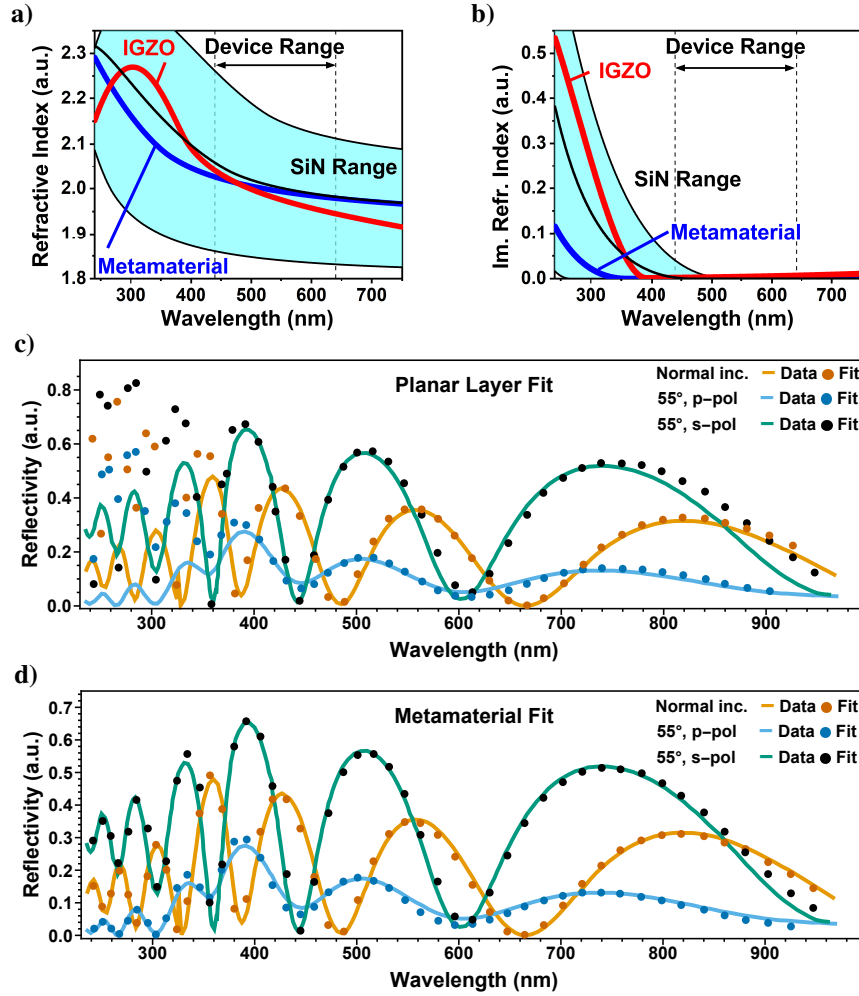
Fig. 2. a) Refractive index (n) data of the metamaterial and its constituent materials measured by ellipsometry. b) Refractive index (k) data of the metamaterial and its constituent materials measured by ellipsometry. c) Scatterometry measurement fitted with a planar layer model. d) Scatterometry measurement fitted with a model having embedded pillar electrodes.

in Figure 2 a) and b). That said, even for this best case scenario, the metamaterial fit remains rather poor and yields an imaginary refractive index that does not align with its constituents. The fit worsens when the thickness is included as fitting parameter. Here, the model gives a significantly lower refractive index (both real and imaginary), paired with a larger thickness of 460nm. (See Supplemental Document) This is a rather unrealistic result, indicating that the inclusion of IGZO inside a SiN matrix can no longer be fitted with an isotropic model. It should, however, not be a surprise that an anisotropic metamaterial can not be fitted with an isotropic model. In fact, only at the wavelength where the 2 materials are equal an isotropic model succeeds. Evidently, a more advanced optical model is needed to extract correct parameters for which we look towards scatterometry and Mueller matrix measurements.

3.1.2. Scatterometry

Scatterometry measurements (Nova T600 MMSR) and fits (Nova Mars) were performed on the finished metamaterial, shown in Figure 2 c) - d). The earlier mentioned refractive indices were used as input to extract the parameters of the embedded IGZO electrode in the SiN matrix.

Figure 2 c) shows the measured data (full line) and a structural fit (points) that represents the metamaterial by a single SiN layer without embedded electrodes. The fit indicates that this unpatterned layer should be 411nm thick, which aligns well with the SEM data. For all wavelengths above 400nm, the model correspondents well with the measured data. At wavelengths below 400nm, due to the growing difference in SiN and IGZO refractive indexes, we are not expecting to obtain a fit in that spectral range. Figure 2 d) shows the same measurement data, now fitted with a model that assumes a SiN layer with embedded IGZO electrodes. The fit indicates a metamaterial thickness, pillar height and pillar width of 408nm, 423nm and 74nm respectively. For this second model, the complete wavelength range was fitted well, showcasing that the created metamaterial matches with the design and the measured SEM data.

Table 3. Overview of metamaterial structural parameters fitted by scatterometry.

Model	Thickness (nm)	Pillar Width (nm)
SEM	420	45nm
Metamaterial ellipsometry	420-460	NA
Scatterometry (planar layer)	411	NA
Scatterometry (metamaterial fit)	408 - 423	74

3.1.3. Rigorous Coupled Wave Analysis

RCWA models were created and their structural parameters were fit to averaged Mueller matrix (MM) ellipsometry measurements (Woollam RC2 - averaged from 30 measurements at 75° incidence). The ellipsometry data from Figure 2 was used as input during the fits. A fitting algorithm was created, based on pySCATMECH for calculating Mueller matrices and a robust Least Square (LSQ) fitting function for optimizing the model. [37, 38] The LSQ functions $F(\mathbf{x})$ is defined as:

$$F(\mathbf{x}) = \sum_{j=1}^{m} \frac{(y_j - f_j(\mathbf{x}))^2}{\sigma_j^2} \tag{1}$$

Here, $\mathbf{x}$ is a vector representing the RCWA structural parameters, y_j represents the measured MM datapoints at the j-th wavelength, $f_j(\mathbf{x})$ are the calculated datapoints by the RCWA model and σ_j^2 is the variance of 30 separate measurements. Figure 3 a) shows a schematic of the RCWA models that were fitted to the measured MM data. Two fits were made with: (1) a model based on a single SiN layer and (2) a model that assumes the metamaterial has 45nm sized embedded electrodes in a SiN matrix having 90nm pitch. The pillar width and pitch were not fitted since the model has only a negligible sensitivity to them. (See Supplemental Document) The fits and measured MM data are shown in Figure 3 b). It should be noted that MM data is usually normalized to the first element (MM11) and that there are eight zero elements due to the symmetry of the measured metamaterial structure. [39]
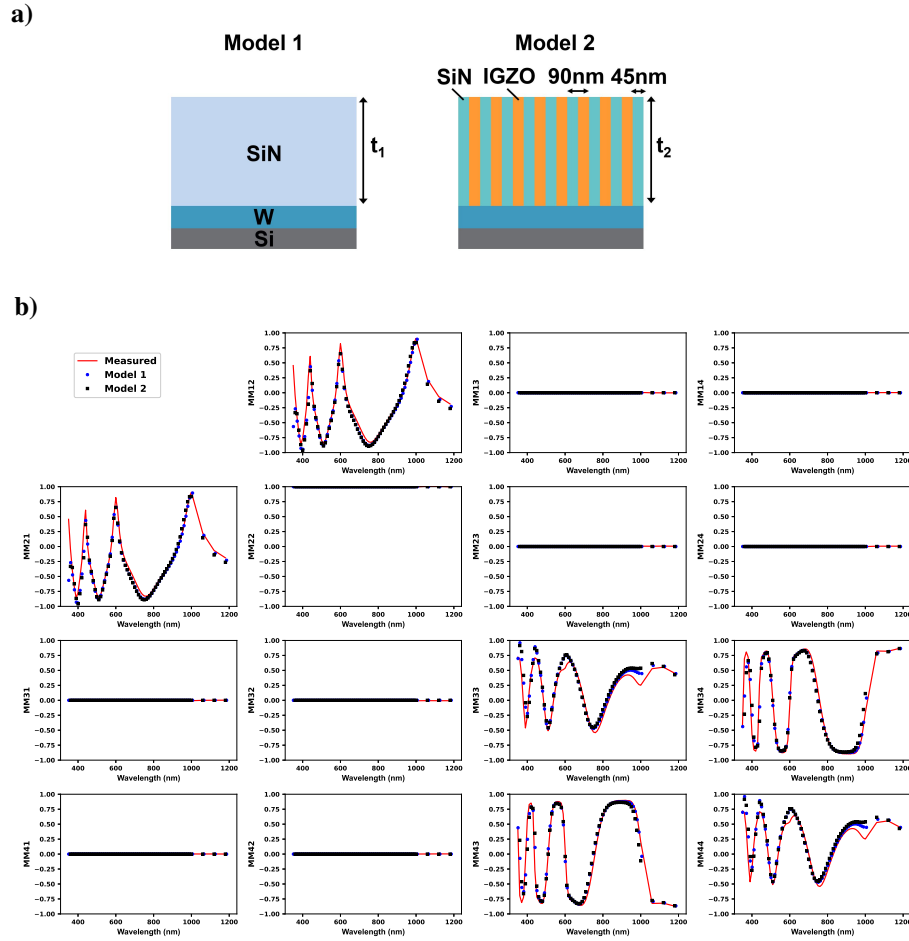
Fig. 3. a) Schematic of the RCWA model assuming the metamaterial is an effective medium. b) Schematic of the RCWA model having IGZO pillars embedded in SiN. c) Mueller matrix measurement and fits of the various models shown in a)-b).

For model 1, a good fit with an LSQ value of 4132 was achieved resulting in a thickness of 422nm, proving accurate calculation of the MM data and matching well with our SEM data. For model 2, which matches the designed ideal metamaterial (45nm electrodes with 90nm pitch), an LSQ value of 5797 was found at a thickness of 424nm compared to model 1. Clearly, both models fit the thickness of the metamaterial well. (See Table 4) The closely matching LSQ values confirm the isotropic nature of the metamaterial. See Supplemental Document for the LSQ values for various fitted metamaterial heights.

3.2. Electrical Characterization

To prove the conductivity of the metamaterial, conductive atomic force microscopy (C-AFM) measurements were performed. Figure 4 shows a comparison between an atomic force microscopy (AFM) and C-AFM measurement. AFM data confirms that the electrode pillar slightly (~ 11nm) extrudes from the metamaterial after planarization which aligns well with our SEM data. Figure 4 b) shows a schematic of the electric loop connecting the back contact, pillar electrodes and

Table 4. Overview of metamaterial strucural parameters fitted by RCWA simulations.

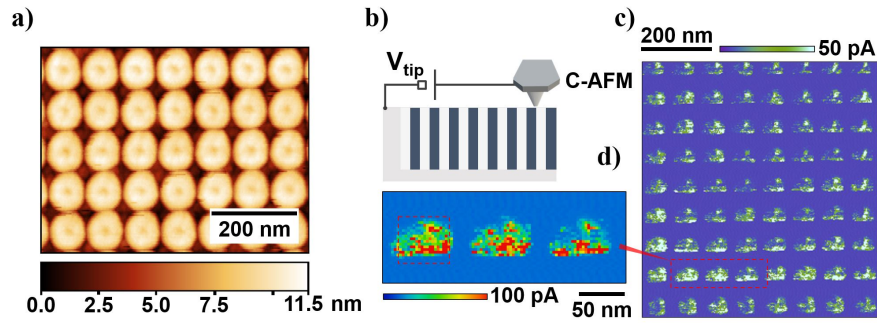| Model	Thickness (nm)	Pillar Width (nm)
SEM	420	45nm
Metamaterial ellipsometry	420-460	NA
RCWA (planar fit)	422	NA
RCWA (metamaterial fit)	424	No sensitivity

Fig. 4. a) Relative height image of metamaterial by atomic force microscope. b) Schematic of conductive atomic force microscope operation. c) Current map of individual metamaterial pillars by conductive atomic force microscope. d) High resolution conductive atomic force microscope image of the metamaterial.

the C-AFM. Here, a nanosized conductive probe is scanned in direct contact with the sample surface while a voltage is applied between the tip and the sample. Note, that although the probe is scanning the surface in direct contact, a relatively high tip-sample contact resistance exists between the tip and the IGZO resulting in low detectable leakage (i.e., in the pA range). Furthermore, the observed conduction is linked to a convolution of all the present resistive terms. Hence, this is a combination of the electrode pillar, the metallic back contact and the Si substrate. Consequently, the dominant resistance is not the tip-sample junction and the absolute value of current measured should only be considered in relative terms. Additionally, local fluctuations must be ascribed to small surface modifications of the IGZO top surface such as stoichiometry variations or intra-grains scattering that can locally make the resistance of the tip-sample junction dominant. Figure 4 c) shows current flowing at the tip-sample junction when scanning with 6V bias over an area of 0.8 x 0.8 μm^2. Clear contrast is visible corresponding to IGZO, indicating a lower resistance path for current in these locations and thus confirming the electrode conductivity. The observed non-round pillar shape is likely linked to the larger than normal employed C-AFM tip pressure in an attempt to minimize the tip sample resistive junction. Consequently, the slightly triangular shape is clearly the result of a truncated probe scanned at high pressure, thus losing the high aspect ratio of a pristine conductive probe. Higher resolution C-AFM imaging is reported in Figure 4 d) where three IGZO pillars are sensed. The results indicate that the electrical properties of the IGZO pillars are not uniform, with clear variations of the measured leakage with fluctuations in the range of 10-20 nm. These are attributed to local structural, and compositional variations.

4. Conclusion

We have presented a metamaterial electrode cladding layer designed for waveguide based optical modulators. Three criteria were identified that make for an excellent electrode cladding. Hence, no metals were used close to the active region, a subwalenght electrode pitch was used and Bragg scattering was avoided by refractive index matching the constituent materials, namely SiN and IGZO. We have shown ellipsometry measurements and fits of the metamaterial and its constituents and conclude that it behaves optically isotropic over the visible range. We find that standard ellipsometry oscillators result in a poor fit on the metamaterial, evident from its lower than expected imaginary refractive index. This problems exacerbates when the thickness is included as fitting parameter resulting in a thicker layer with a lowered real refractive index. On the other hand, scatterometry and MM RCWA measurements confirm the dimensions of the embedded pillars and the metamaterial respectively. AFM indicates that the pillar electrodes extrude slightly from its SiN matrix and C-AFM confirms the conductivity of the pillar electrodes. A similar fabrication scheme can be used with alternative materials expanding the capabilities of the metamaterial into different operating regimes, for example ITO can lead to faster switching speeds due to its higher carrier concentration compared to IGZO.

5. Backmatter

Disclosures. The authors have nothing to disclose.

Data availability. Data underlying the results presented in this paper are available in Dataset 1, Ref. [3].

Supplemental document. See Supplement 1 for supporting content.

References

1. Q. Jiang, G. Jin, and L. Cao, "When metasurface meets hologram: principle and advances," Adv. Opt. Photonics **11**, 518 (2019).
2. J. Sun, E. Timurdogan, A. Yaacobi, E. S. Hosseini, and M. R. Watts, "Large-scale nanophotonic phased array," Nature **493**, 195–199 (2013).
3. Z. Ren, Y. Chang, Y. Ma, K. Shih, B. Dong, and C. Lee, "Leveraging of MEMS Technologies for Optical Metamaterials Applications," (2020).
4. W. M. Zhu, A. Q. Liu, X. M. Zhang, D. P. Tsai, T. Bourouina, J. H. Teng, X. H. Zhang, H. C. Guo, H. Tanoto, T. Mei, G. Q. Lo, and D. L. Kwong, "Switchable Magnetic Metamaterials Using Micromachining Processes," Adv. Mater. **23**, 1792–1796 (2011).
5. S. Savo, D. Shrekenhamer, W. J. Padilla, S. Savo, D. Shrekenhamer, and W. Padilla, "Liquid Crystal Metamaterial Absorber Spatial Light Modulator for THz Applications," Adv. Opt. Mater. (2014).
6. Z. He, F. Gou, R. Chen, K. Yin, T. Zhan, and S.-T. Wu, "Liquid Crystal Beam Steering Devices: Principles, Recent Advances, and Future Developments," Crystals **9**, 292 (2019).
7. F. Ding, Y. Yang, and S. I. Bozhevolnyi, "Dynamic Metasurfaces Using Phase-Change Chalcogenides," Adv. Opt. Mater. **7** (2019).
8. S. Y. Lee, Y. H. Kim, S. M. Cho, G. H. Kim, T. Y. Kim, H. Ryu, H. N. Kim, H. B. Kang, C. Y. Hwang, and C. S. Hwang, "Holographic image generation with a thin-film resonance caused by chalcogenide phase-change material," Sci. Reports **7** (2017).
9. J. Hu, S. Bandyopadhyay, Y. H. Liu, and L. Y. Shao, "A Review on Metasurface: From Principle to Smart Metadevices," Front. Phys. **8**, 502 (2021).
10. X. Zhao, Z. Sun, L. Zhang, Z. Wang, R. Xie, J. Zhao, R. You, and Z. You, "Review on Metasurfaces: An Alternative Approach to Advanced Devices and Instruments," Adv. Devices & Instrumentation **2022**, 1–19 (2022).
11. C. Cho, T. Antrack, M. Kroll, Q. An, T. R. Bärschneider, A. Fischer, S. Meister, Y. Vaynzof, and K. Leo, "Electrical Pumping of Perovskite Diodes: Toward Stimulated Emission," Adv. Sci. **8** (2021).
12. M. Ferrera, S. Saha, A. Boltasseva, V. M. Shalaev, and W. Jaffray, "Transparent conducting oxides: from all-dielectric plasmonics to a new paradigm in integrated photonics," Adv. Opt. Photonics, Vol. 14, Issue 2, pp. 148-208 **14**, 148–208 (2022).

13. V. E. Babicheva, A. Boltasseva, and A. V. Lavrinenko, "Transparent conducting oxides for electro-optical plasmonic modulators," Nanophotonics **4**, 165–185 (2015).

14. M. Dasog, "Transition Metal Nitrides Are Heating Up the Field of Plasmonics," Chem. Mater. **34**, 4249–4258 (2022).

15. M. Gioti, J. Arvanitidis, D. Christofilos, K. Chaudhuri, T. Zorba, G. Abadias, D. Gall, V. M. Shalaev, A. Boltasseva, and P. Patsalas, "Plasmonic and phononic properties of epitaxial conductive transition metal nitrides," J. Opt. **22**, 084001 (2020).

16. G. V. Naik, V. M. Shalaev, and A. Boltasseva, "Alternative Plasmonic Materials: Beyond Gold and Silver," Adv. Mater. **25**, 3264–3294 (2013).

17. E. Feigenbaum, K. Diest, and H. A. Atwater, "Unity-Order Index Change in Transparent Conducting Oxides at Visible Frequencies," Nano Lett. **10**, 2111–2116 (2010).

18. G. V. Naik, J. Kim, and A. Boltasseva, "Oxides and nitrides as alternative plasmonic materials in the optical range [Invited]," Opt. Mater. Express **1**, 1090 (2011).

19. Y.-W. Huang, H. W. H. Lee, R. Sokhoyan, R. A. Pala, K. Thyagarajan, S. Han, D. P. Tsai, and H. A. Atwater, "Gate-Tunable Conducting Oxide Metasurfaces," Nano Lett. **16**, 5319–5325 (2016).

20. J. Kim, S. Choudhury, C. DeVault, Y. Zhao, A. V. Kildishev, V. M. Shalaev, A. Alù, and A. Boltasseva, "Controlling the Polarization State of Light with Plasmonic Metal Oxide Metasurface," ACS Nano **10**, 9326–9333 (2016).

21. J. Park, J.-H. Kang, S. J. Kim, X. Liu, and M. L. Brongersma, "Dynamic Reflection Phase and Polarization Control in Metasurfaces," Nano Lett. **17**, 407–413 (2017).

22. M. Y. Shalaginov, S. D. Campbell, S. An, Y. Zhang, C. Ríos, E. B. Whiting, Y. Wu, L. Kang, B. Zheng, C. Fowler, H. Zhang, D. H. Werner, J. Hu, and T. Gu, "Design for quality: Reconfigurable flat optics based on active metasurfaces," Nanophotonics **9**, 3505–3534 (2020).

23. R. W. Ziolkowski, "Propagation in and scattering from a matched metamaterial having a zero index of refraction," Phys. Rev. E **70**, 046608 (2004).

24. I. Liberal and N. Engheta, "Near-zero refractive index photonics," Nat. Photonics **11**, 149–158 (2017).

25. X. Niu, X. Hu, S. Chu, and Q. Gong, "Epsilon-Near-Zero Photonics: A New Platform for Integrated Devices," Adv. Opt. Mater. **6**, 1701292 (2018).

26. H. W. Lee, G. Papadakis, S. P. Burgos, K. Chander, A. Kriesch, R. Pala, U. Peschel, and H. A. Atwater, "Nanoscale conducting oxide PlasMOStor," Nano Lett. **14**, 6463–6468 (2014).

27. I. C. Reines, M. G. Wood, T. S. Luk, D. K. Serkland, and S. Campione, "Compact epsilon-near-zero silicon photonic phase modulators," Opt. Express **26**, 21594 (2018).

28. D. C. Zografopoulos, G. Sinatkas, E. Lotfi, L. A. Shahada, M. A. Swillam, E. E. Kriezis, and R. Beccherelli, "Amplitude modulation in infrared metamaterial absorbers based on electro-optically tunable conducting oxides," Appl. Phys. A: Mater. Sci. Process. **124** (2018).

29. E. H. Turner, "High-Frequency Electro-Optic Coefficients of Lithium Niobate," Appl. Phys. Lett. **8**, 303–304 (1966).

30. C. Wang, M. Zhang, B. Stern, M. Lipson, and M. Lončar, "Nanophotonic lithium niobate electro-optic modulators," Opt. Express **26**, 1547 (2018).

31. S. Abel, T. Stöferle, C. Marchiori, C. Rossel, M. D. Rossell, R. Erni, D. Caimi, M. Sousa, A. Chelnokov, B. J. Offrein, and J. Fompeyrine, "A strong electro-optically active lead-free ferroelectric integrated on silicon," Nat. Commun. **4**, 1671 (2013).

32. S. Steudel, J. L. P. Van Der Steen, M. Nag, T. H. Ke, S. Smout, T. Bei, K. van Diesen, G. de Haas, J. Maas, J. de Riet, M. Rovers, R. Verbeek, Y. Y. Huang, S. C. Chiang, M. Ameys, F. de Roose, W. Dehaene, J. Genoe, P. Heremans, G. Gelinck, and A. J. Kronemeijer, "Power saving through state retention in IGZO-TFT AMOLED displays for wearable applications," Dig. Tech. Pap. - SID Int. Symp. **48**, 38–41 (2017).

33. A. V. Glushkova, H. F. W. Dekkers, M. Nag, J. I. del Agua Borniquel, J. Ramalingam, J. Genoe, P. Heremans, and R. Rolin, "Systematic Study on the Amorphous, C-Axis-Aligned Crystalline, and Protocrystalline Phases in In–Ga–Zn Oxide Thin-Film Transistors," ACS Appl. Electron. Mater. **3**, 1268–1278 (2021).

34. A. de Jamblinne de Meux, A. Bhoolokam, G. Pourtois, J. Genoe, and P. Heremans, "Oxygen vacancies effects in a-IGZO: Formation mechanisms, hysteresis, and negative bias stress effects," physica status solidi (a) **214**, 1600889 (2017).

35. G. E. Jellison and F. A. Modine, "Parameterization of the optical functions of amorphous materials in the interband region," Appl. Phys. Lett. **69**, 371–373 (1996).

36. T. E. Tiwald, D. W. Thompson, J. A. Woollam, W. Paulson, and R. Hance, "Application of IR variable angle spectroscopic ellipsometry to the determination of free carrier concentration depth profiles," Thin Solid Films **313-314**, 661–666 (1998).

37. T. A. Germer, "pySCATMECH: A Python interface to the SCATMECH library of scattering codes," in *Reflection, Scattering, and Diffraction from Surfaces VII,* vol. 11485 L. M. Hanssen, ed. (SPIE, 2020), p. 17.

38. J. Zhu, S. Liu, X. Chen, C. Zhang, and H. Jiang, "Robust solution to the inverse problem in optical scatterometry," Opt. Express **22**, 22031 (2014).

39. O. Arteaga, "Useful Mueller matrix symmetries for ellipsometry," Thin Solid Films **571**, 584–588 (2014).